Robotica (2025), **43**, pp. 3155–3175
doi:10.1017/S0263574725102105

CAMBRIDGE UNIVERSITY PRESS

RESEARCH ARTICLE

Robotic gripper for dynamic capture using passive variable stiffness and damping regulator (P-VSDR)

Shangkui Yang[1], Zhibin Song[1], David T. Branson[2], Tao Sun[1], Jian S. Dai[3] and Rongjie Kang[1]

[1]Key Laboratory of Mechanism Theory and Equipment Design of Ministry of Education, School of Mechanical Engineering, Tianjin University, Tianjin, P.R. China
[2]Advanced Manufacturing Technology Research Group, Faculty of Engineering, University of Nottingham, Nottingham, UK
[3]Shenzhen Key Laboratory of Intelligent Robotics and Flexible Manufacturing Systems, Southern University of Science and Technology, Shenzhen, P.R. China
Corresponding author: Rongjie Kang; Email: rjkang@tju.edu.cn

Received: 4 April 2025; **Revised:** 3 June 2025; **Accepted:** 12 July 2025; **First published online:** 27 August 2025

Keywords: robotic gripper; dynamic capture; stiffness; damping

Abstract

Capturing dynamic targets is particularly challenging for either rigid or soft grippers, as impact buffering should be completed in a short time to ensure the reliability of the robotic system. At collision onset, to deal with relatively low contact forces, adopting low stiffness and damping can effectively mitigate the rebound of the dynamic targets. As the contact area and forces increase, employing high stiffness and damping becomes necessary for absorbing high energy. This paper proposed a novel robotic gripper whose stiffness and damping follow a predefined profile "low stiffness and damping for low impact and high stiffness and damping for high impact." The variable effects of impact buffering and energy dissipation in a collision process were modeled and analyzed. Then, a passive variable stiffness and damping regulator (P-VSDR) was developed where tendons and pulleys are used to generate a nonlinear motion from a linear spring-damper unit. The contact dynamics model of the robotic gripper equipped with P-VSDR was established. Simulated and experimental results show that this gripper enables reliable capture of dynamic targets with different velocities.

1. Introduction

Capturing dynamic targets is a challenging task, requiring highly developed physical structures and nervous systems. For instance, a well-trained baseball player can capture a flying ball through eye-hand-body coordination [1]. When the biological systems come into contact or collision with dynamic targets, they utilize soft tissues (e.g., ligament and muscle) around the biological joints (e.g., shoulder and elbow), to deal with the impact force, ensuring their safety and stability [2–4]. At the beginning of contact or collision, compliant interaction is required to mitigate local stress concentrations and overloading, preventing the rebound of dynamic targets. As the contact area expands and impact force intensifies, higher stiffness and damping are required to absorb and dissipate the energy, avoiding serious structural deformation or failure. According to biomechanics, the stiffness and damping of the soft tissues have a dependence on the extent to which they are stretched [5]. This variable mechanism optimizes the dynamic response of biological systems under varying impact conditions [6], which can be summarized as "low stiffness and damping for low impact and high stiffness and damping for high impact." In other words, biological systems can soften to perform actions requiring compliance and stiffen to bear a heavy impact load [7].

Various works have been done to transfer the biological features to robotic grippers, yet most of them have focused on grasping static or quasi-static targets [8]. The rigid ones, integrated with high-performance sensors and sophisticated active control algorithms, exhibited excellent performance in

© The Author(s), 2025. Published by Cambridge University Press.

https://doi.org/10.1017/S0263574725102105 Published online by Cambridge University Press

terms of controllability and load capacity [9–11]. Nonetheless, strong impacts during collisions may cause damage to the rigid robotic systems [12]. Moreover, a slight deviation in positioning or orientation may lead to undesired collision and bounce of the dynamic targets, resulting in capture failure [13]. In the field of soft robotics [14, 15], researchers utilized soft materials (such as silicone rubber [16], hydrogels [17], polyurethane [18], etc.) to design various functional soft robots (such as grasping [19], swimming [20], jumping [21], etc.). They are expected to exhibit effective interaction in environmental settings. Like biological joints relying on soft tissues to reduce impacts, soft robots essentially do the same [22]. Sinatra et al. developed an ultra-lightweight soft robotic gripper capable of nondestructive grasping and manipulation of fragile marine life such as jellyfish [23]. This gripper achieves very low contact pressure through nanofiber-reinforced soft actuators, ensuring minimal harm to jellyfish species. Lin et al. developed a Venus flytrap-inspired soft gripper that can grasp fast-moving tennis balls by utilizing snap-through instability and trigger structures [24]. In our previous research, a multi-tentacle gripper inspired by a sea anemone was proposed to capture dynamic targets [1, 25, 26].

To endow soft robots with the ability to adapt to different loading conditions [27], adjustable stiffness or damping mechanisms/materials have been developed in recent years [28–34], such as jamming mechanisms, antagonistic mechanisms, and smart materials. Despite some advances in the research of soft grippers to grasp heavy objects [35], they are not comparable to biological systems in effectively buffering impacts when colliding with dynamic targets. The task of capturing dynamic targets requires fast perception of impact forces and real-time adjustment of stiffness and damping. In terms of perception, active detection, for example, embedded sensors, will encounter limitations in bandwidth constraints [36]. In terms of actuation, although compliant/soft structures can provide good buffering performance, they lead to slow response to capture dynamic targets [37].

For a robotic system to capture dynamic targets with high kinetic energy, strong contact interaction is inevitable. The contact problem is characterized by a large range of velocity variation, short duration of contact, and great impact force [38]. Consequently, a thorough analysis of the contact dynamics is essential prior to the design of robotic grippers [39]. At present, many contact models have been proposed, taking the Hertz model as the theoretical basis [40]. A commonly used contact force model considering the damping loss is the Kelvin–Voigt model, which used a linear damping to measure the energy loss [41]. Moreover, a number of nonlinear spring and damping models were proposed, which took material properties, geometry of contact surfaces, elastic compression, and initial contact velocities into consideration. Among these models, the Hunt–Crossley model can effectively explain the buffering of impact forces and the dissipation of energy during the impact contact process [42].

This paper proposes a passive variable stiffness and damping regulator (P-VSDR) that can be integrated into a robotic gripper and demonstrates its potential in impact buffering scenarios. The main contributions include: (1) This study reveals the nonlinear effects of stiffness and damping during the contact and collision to absorb the kinetic energy. A predefined profile for variable stiffness and damping enables low stiffness and damping for low impact scenarios and high stiffness and damping for high impact scenarios. (2) A P-VSDR, engineered as an impact buffer for a tendon-driven robotic gripper, is proposed. The P-VSDR utilizes passive nonlinear dynamics to enhance the buffering performance and response speed of the robotic gripper in handling dynamic targets.

The subsequent sections of this paper are organized as follows: Section 2 elucidates the fundamental principles governing impact contact dynamics. The mechanical design of the P-VSDR and the development of the robotic gripper prototype are detailed in Section 3. Section 4 establishes the kinematic and dynamic models for the gripper integrated with the P-VSDR. Subsequent to this, Section 5 presents a series of experiments to validate the performance of the proposed prototype. Conclusion and discussion are presented in Section 6.

2. Principle of the impact contact

In this section, the principle of variable stiffness and damping during contact is investigated to guide the design of the robotic gripper used for dynamic capture. The impact force under constant and variable

https://doi.org/10.1017/S0263574725102105 Published online by Cambridge University Press

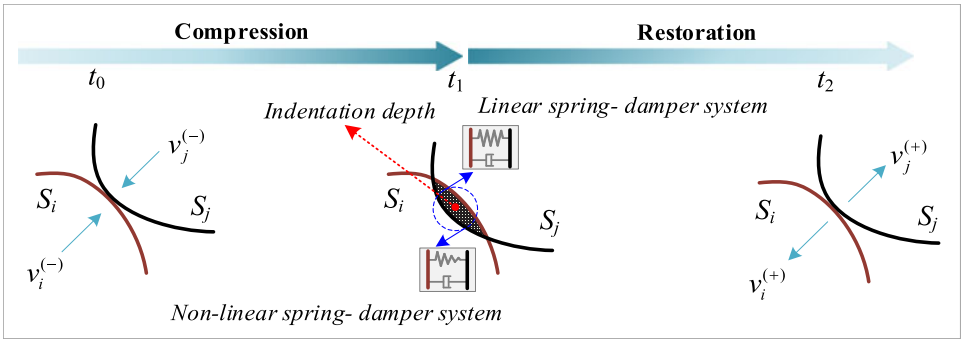


Figure 1. *The elastic compression and restoration process of two contacting surfaces.*

Table I. *Mathematical descriptions and properties of the contact dynamic models.*

Model	Mathematical descriptions		Properties
Kelvin–Voigt model [41]	$F_n = Kx + D\dot{x}$	(1)	Constant stiffness and damping
Hunt–Crossley model [42]	$F_n = Kx^n \left[1 + \frac{3(1-Cr)}{2} \frac{\dot{x}}{\dot{x}_0}\right]$	(2)	Variable stiffness and damping

stiffness and damping conditions was modeled based on two classical contact models: the Kelvin–Voigt and Hunt–Crossley models, as summarized in Table I.

2.1. Modeling of the impact force

The contact process was described by using a linear viscoelastic method (the Kelvin–Voigt model) and a nonlinear one (the Hunt–Crossley model), respectively. Figure 1 shows the elastic compression and restoration phases between two contacting surfaces of the objects, S_i and S_j. The indentation depth where the surfaces come into contact can be equivalently regarded as either a linear or nonlinear spring-damper system depending on the material properties [43]. In the elastic compression phase from time t_0 to t_1, the relative velocity gradually decreases, and the contact force gradually increases. The maximum contact force occurs at time t_1. In this process, part of the kinetic energy of the objects was stored in the spring, and the other part was dissipated by the damping. In the elastic restoration phase from time t_1 to t_2, the deformation between the contact objects starts to restore, and the contact force gradually decreases until it becomes 0 at time t_2. In this process, part of the elastic potential energy in the spring was converted into the kinetic energy of the objects, and the other part was dissipated through damping.

In the Kelvin–Voigt and Hunt–Crossley models, the contact stiffness between the contacting surfaces S_i and S_j can be determined by considering their material properties and radius d of contact geometry. Assuming the Young's modulus of S_i and S_j are E_i and E_j, and the Poisson's ratios are ν_i and ν_j, respectively. The contact stiffness K between two contacting surfaces of objects is

$$K = \frac{4E_iE_j}{3\left(1-\nu_i^2\right)E_i + \left(1-\nu_j^2\right)E_j}\sqrt{\frac{d_id_j}{d_i+d_j}} \tag{3}$$

The effective mass is

$$M = \frac{m_im_j}{m_i+m_j} \tag{4}$$

where m_i and m_j represent the mass of S_i and S_j, respectively.

https://doi.org/10.1017/S0263574725102105 Published online by Cambridge University Press

Table II. *List of simulation parameters in contact reaction.*

Symbol	Description	Value
m_i	Mass of the S_i	50 g
m_j	Mass of the S_j	100 g
$v_{i,0}$	Initial velocity of the S_i	3 m/s
$v_{j,0}$	Initial velocity of the S_j	0 m/s
$\dot{x}_0$	The initial relative velocity	3 m/s
E_i	The elastic modulus of the S_i	5 Mpa
E_j	The elastic modulus of the S_j	5 Mpa
d_i	Radius of the S_i	5 mm
d_j	Radius of the S_j	15 mm
ν_i	Poisson's ratio of the S_i	0.48
ν_j	Poisson's ratio of the S_j	0.48
Cr	The restitution coefficient	0.5
ζ	Damping ratio of the spring-damper system	0.1

The damping coefficient of a spring-damper system describes the ability of energy dissipation during an impact process. The damping coefficient D can be calculated by

$$D = 2\zeta\sqrt{KM} \tag{5}$$

where ζ is the damping ratio of the spring-damper system.

In the Hunt–Crossley model, C_r is the restitution coefficient during the contact process, $\dot{x}_0$ is the relative initial velocities, and n is a nonlinear coefficient related to the material itself, typically taken as 1.5 [42].

2.2. Analysis of the impact force

Numerical simulation of the contact process was performed based on the Kelvin–Voigt and Hunt–Crossley contact models, respectively. Here, we consider a scenario that the contact occurs between two spheres made of rubber, because rubber is a typical elastic material that can be characterized by the contact models. The parameters are presented in Table II.

Figure 2 illustrates the simulation results of impact buffering and energy dissipation, under the constant stiffness-damping conditions by using the Kelvin–Voigt model and the variable stiffness-damping conditions by using the Hunt–Crossley model. Figure 2(a) shows the impact force F_n exhibiting a hysteresis loop. The area enveloped by the impact and restoration curves indicates the dissipated energy. When the two surfaces initially contact, the positive relative velocity $\dot{x}$ results in a positive damping force, while the indentation depth x is zero and the corresponding spring force is zero, causing the initial state of the impact force F_n in the Kelvin–Voigt model to offset from the origin. Figure 2(b) illustrates the damping and stiffness as functions of indentation. It can be seen that a constant stiffness (8000 N/m) and a constant damping (3.2 Ns/m) are utilized in the Kelvin–Voigt model, while variable stiffness (increasing to approximately 1000N/m) and damping (increasing to approximately 4 Ns/m) are employed in the Hunt–Crossley model.

Figure 2(c) presents a comparative analysis of the impact force F_n across different models. During the contact process between the spheres S_i and S_j, the maximum impact force in the Kelvin–Voigt model reaches 43 N, with an approximate duration of contact of 0.006 s. However, in the Hunt–Crossley model, the maximum impact force is 18 N, with a duration of contact of about 0.02 s. In contrast to the constant stiffness of the Kelvin–Voigt model, the Hunt–Crossley model exhibits a superior ability to reduce peak impact forces and extend the duration of contact. These characteristics are crucial for mitigating the

https://doi.org/10.1017/S0263574725102105 Published online by Cambridge University Press

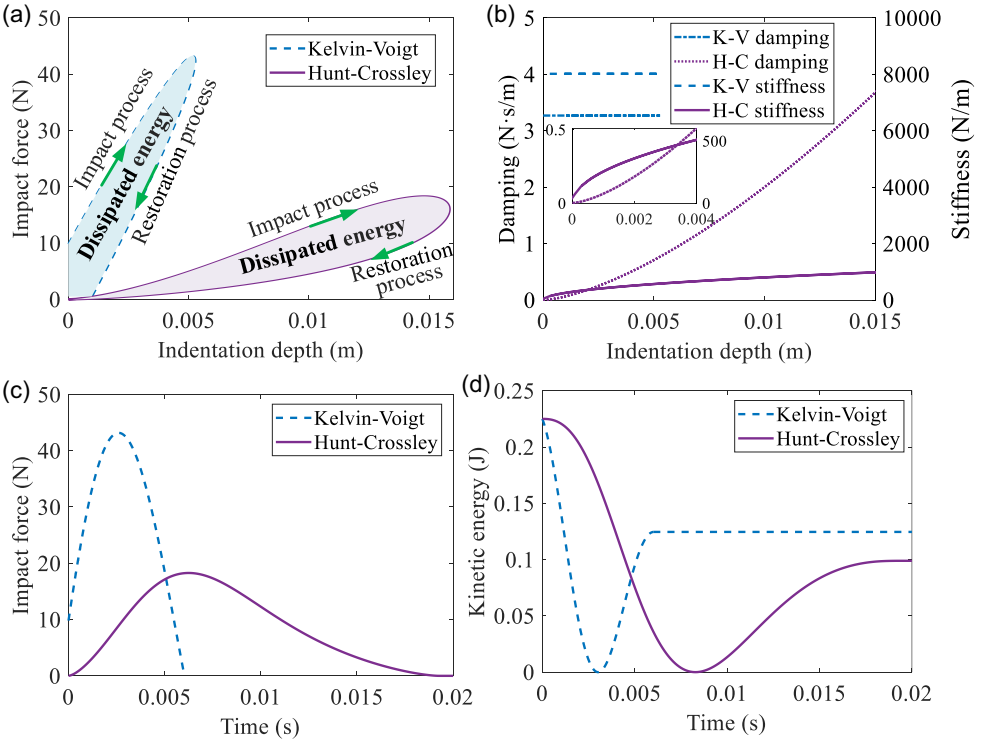


Figure 2. *Comparison of contact dynamics: constant stiffness-damping (Kelvin–Voigt model) versus variable stiffness-damping (Hunt–Crossley model). (a) Impact force and dissipated energy with respect to indentation depth. (b) Variation of stiffness and damping in the two models. (c) Impact force as a function of time. (d) Kinetic energy of the dynamic target as a function of time.*

detrimental effects of impact force, enabling more effective energy distribution and dissipation throughout the collision process. This results in a more robust resistance to the potential for damage caused by dynamic loading conditions

The effects of variable stiffness and damping are also demonstrated from the viewpoint of energy. The ratio between the $K_{i,0}$–K_i and corresponding $K_{i,0}$ is used to characterize the kinetic energy dissipation efficiencies η, as shown in Eq. (6).

$$K_{i,0} = \frac{1}{2} m_i {v_{i,0}}^2, \quad K_i = \frac{1}{2} m_{i,0}{}^2, \quad \eta = \frac{K_{i,0} - K_i}{K_{i,0}} \times 100\% \tag{6}$$

where $K_{i,0}$ is the initial kinetic energy of the S_i at the time of impact, K_i is the kinetic energy of the S_i at the time of separation, and $K_{i,0}$–K_i is the dissipated kinetic energy of the S_i at the time of separation. Figure 2(d) compares the kinetic energy of the dynamic target S_i obtained by the Kelvin–Voigt and Hunt–Crossley models. The dynamic target S_i initially had a kinetic energy of 0.225J and was reduced to 0.125J by using the Kelvin–Voigt model, with the kinetic energy dissipation efficiency of 44.4%. However, the kinetic energy of the dynamic target was reduced to 0.098J by using the Hunt–Crossley model, with the kinetic energy dissipation efficiency of 56.4%. Compared to the constant damping characteristic of the Kelvin–Voigt model, the Hunt–Crossley model effectively enhances energy dissipation and extends the duration of impact engagement. This improved energy dissipation capacity plays a critical role in suppressing impact oscillations, thereby contributing to a more stable response for dynamic capture.

In the context of the Hunt–Crossley model, the deceleration in the increasing rate of stiffness during collision effectively prolongs the interaction time between objects, consequently attenuating peak impact forces. Simultaneously, the accelerated increase in damping reduces the elastic potential energy and enhances energy dissipation. This variable stiffness and damping approach, in contrast to a constant

https://doi.org/10.1017/S0263574725102105 Published online by Cambridge University Press

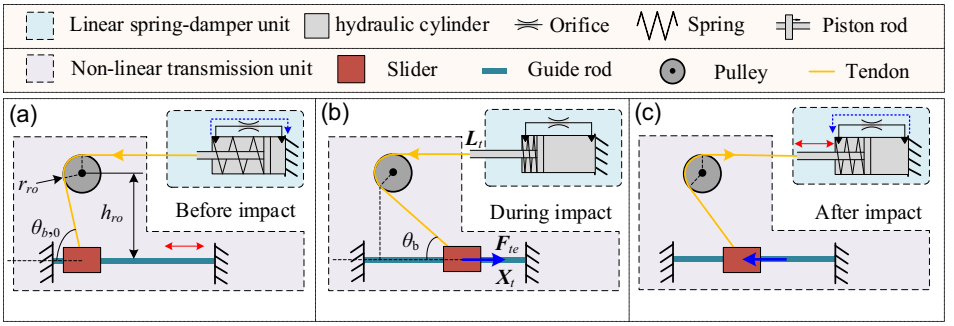


Figure 3. *Working principle of the P-VSDR. (a) The initial state with no external impact load. (b) The compressing state due to external impact load* $\boldsymbol{F}_{te}$*. (c) The restoration state when external impact load vanishes.*

stiffness and damping configuration, provides substantial promise for improving impact buffering and energy dissipation for dynamic target capturing. At the beginning of dynamic target capturing, where minimal deformation and low impact forces are prevalent, reduced stiffness and damping help prevent an overly rigid system response, thereby mitigating the risk of target bouncing. As the process progresses into the later stages of dynamic target capturing, characterized by increased deformation and significant impact forces, elevated stiffness and damping become instrumental in expediting energy dissipation and suppressing the tendency for impact resonance.

Leveraging the principles of the Hunt–Crossley model, a tailored variable stiffness and damping mechanism for dynamic target capturing is proposed, inspired by the concept of "low stiffness and damping for low impact and high stiffness and damping for high impact," to guide the design of our gripping mechanism.

3. Principle of the P-VSDR

The primary challenge in constructing a gripper for dynamic capture is to develop a compliant mechanism embedded with variable stiffness and damping. In this section, a P-VSDR was proposed by utilizing a special compliant structure that combines the nonlinear motion of tendons with linear elastic elements. The P-VSDR was then integrated into a robotic gripper to achieve impact buffering and energy dissipation for capturing dynamic targets.

3.1. Design methodology of the P-VSDR

The P-VSDR consists of a linear spring-damper unit and a nonlinear tendon-driven transmission unit, as shown in Fig. 3. The linear spring-damper unit is composed of a hydraulic cylinder and a bypass orifice. The hydraulic cylinder contains a piston rod and a linear spring. The nonlinear transmission unit is composed of a pulley, a guide rod, and a slider. One end of the tendon is fixed to the slider, while the other end is fixed to the piston rod via the pulley. Frictions from pulleys, sliders, and piston rods are reduced by using the ball and linear bearings, as well as the lubrication provided by the hydraulic oil in the cylinder; thus, frictions are assumed to be negligible in comparison to the dynamic impact during the capture process.

When the impact force $\boldsymbol{F}_{te}$ is applied to the slider, the slider moves along the guide rod in the direction of the impact force. At this time, the angle between the tendon and the slider, θ_b, decreases. It is important to note that this change of the angle θ_b is nonlinear. The impact force $\boldsymbol{F}_{te}$ pulls out the piston rod via the tendon, causing the spring to compress and the hydraulic oil to flow back into the right chamber through the orifice. From the viewpoint of energy, the impact energy is partially transferred to the elastic energy in the spring, and partially dissipated by the orifice, as shown in Fig. 3(b). When the impact process is finished, the energy stored in the linear spring will be released, pushing the piston rod to the initial state.

https://doi.org/10.1017/S0263574725102105 Published online by Cambridge University Press

The hydraulic oil returns to the left chamber through the orifice, dissipating part of the energy stored in the linear spring again, thereby allowing the slider to return to its initial position, as shown in Fig. 3(c).

The slider moves along the guide rod with a displacement $\boldsymbol{X}_t$ that can be expressed by the angle θ_b as

$$X_t = r_{ro}\left(\sin\theta_{b,0} - \sin\theta_b\right) + \frac{h_{ro} - r_{ro}\cos\theta_b}{\tan\theta_b} - \frac{h_{ro} - r_{ro}\cos\theta_{b,0}}{\tan\theta_{b,0}} \tag{7}$$

where r_{ro} is the radius of the pulley, h_{ro} is the distance from the center of the pulley to the centerline of the guide rod, and $\theta_{b,0}$ is the initial angle between the tendon and the guide rod.

The geometric relationship between the displacement $\boldsymbol{L}_t$ of the piston rod and the angle θ_b of the guide rod is

$$L_t = \frac{\pi r_{ro}\left(\theta_{b,0} - \theta_b\right)}{180} + \frac{h_{ro} - r_{ro}\cos\theta_b}{\sin\theta_b} - \frac{h_{ro} - r_{ro}\cos\theta_{b,0}}{\sin\theta_{b,0}} \tag{8}$$

The resulting force on the slider is composed of the spring force $\boldsymbol{F}_k$ and hydraulic force $\boldsymbol{F}_d$.

$$F_k = k_s L_t \cos\theta_b \tag{9}$$

$$F_d = \frac{\pi\rho\cos\theta_b R_p{}^2\left(R_p{}^2 - r_p{}^2\right)^2}{2C_d{}^2 r_o{}^4}\left(\left(\dot{L}_{t,0}\right)^2 - \frac{k_s L_t{}^2\left(m_s + m_p\right)}{m_s m_p}\right) \tag{10}$$

Thus, the horizontal force $\boldsymbol{F}_{te}$ on the slider is

$$F_{te} = F_k + F_d \tag{11}$$

where k_s is the stiffness of the liner spring in the left chamber of the hydraulic cylinder, C_d represents the flow coefficient of the hydraulic oil through the orifice of orifice, ρ is the density of the hydraulic oil, R_p is radius of the piston, r_p is radius of the piston rod, r_o is radius of the orifice, and m_s and m_p are the mass of the spring and the piston rod, respectively.

The ratio of the spring force change $\Delta\boldsymbol{F}_k$ to the corresponding slider displacement change $\Delta\,\boldsymbol{X}_t$, as shown in Eq. (12), is used to characterize the output effective stiffness on the slider

$$K_{eff} = \frac{\Delta F_k}{\Delta X_t} \tag{12}$$

The ratio of the damping force change $\Delta\boldsymbol{F}_d$ and the corresponding slider velocities change $\Delta\,\dot{X}_t$, as shown in Eq. (13), is used to characterize the output effective damping coefficient on the slider

$$D_{eff} = \frac{\Delta F_d}{\Delta \dot{X}_t} \tag{13}$$

3.2. Simulated analysis of the variable stiffness and damping

According to Eq. (10)–(13), the variation of the effective stiffness K_{eff} and damping coefficient D_{eff} of the P-VSDR with respect to the geometric parameters (h_{ro}, k_s, and r_o) can be obtained and shown in Figs. 4 and 5.

In Fig. 4(a), the variation in the distance h_{r0} from the pulley center to the guide rod centerline has a negligible effect on the effective stiffness curve (i.e., the X_t–K_{eff} relationship) of the P-VSDR. Conversely, the effective stiffness curve is significantly influenced by the spring stiffness k_s and the orifice radius r_o. It can be seen from Fig. 4(b) and (c) that a decrease in the spring stiffness k_s and an increase in the orifice radius r_o both result in a reduced gradient of the effective stiffness curve. In summary, the effective stiffness of the P-VSDR, K_{eff}, exhibits a nonlinear variation with respect to the displacement of the slider, X_t. Initially, the slope is relatively large. However, as the displacement of the slider increases, the slope of the stiffness decreases. This behavior reflects the capability of the P-VSDR for mitigating peak impact forces and extending the duration of impact engagement, which is essential for capturing dynamic targets.

https://doi.org/10.1017/S0263574725102105 Published online by Cambridge University Press

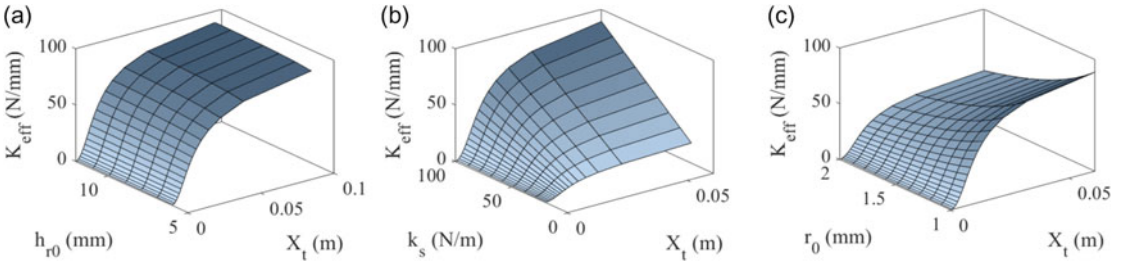


Figure 4. *The effective stiffness K_{eff} of the P-VSDR with respect to structural parameters. (a) distance h_{r0}, (b) spring stiffness k_s, (c) the orifice radius r_0.*

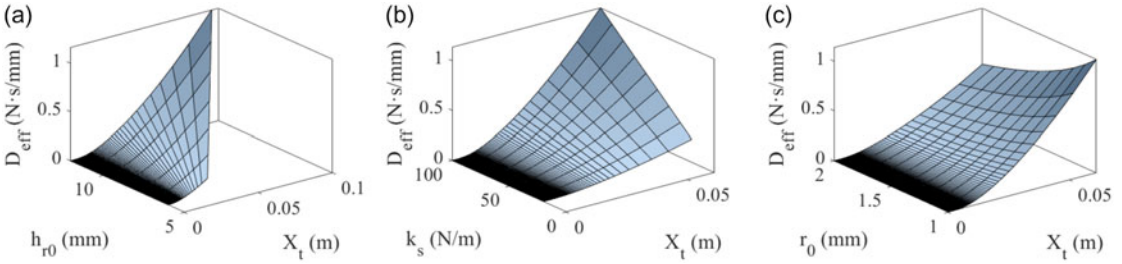


Figure 5. *The damping coefficient D_{eff} of the P-VSDR with respect to structural parameters. (a) distance h_{r0}, (b) spring stiffness k_s, (c) the orifice radius r_0.*

In Fig. 5, the effective damping curve (i.e., the X_t–D_{eff} relationship) is significantly influenced by those structural parameters including the distance h_{r0} from the pulley center to the guide rod centerline, the spring stiffness k_s, and the orifice radius r_o. It can be seen that a decrease in h_{r0}, a reduction in k_s, and an increase in r_o all lead to a decreased gradient of the effective stiffness curve. In summary, Fig. 5 shows that the effective damping of the P-VSDR, D_{eff}, increases with the displacement of the slider, X_t. Unlike stiffness, the damping exhibits an increasing slope, which enhances the energy dissipation capabilities. This characteristic is critical for suppressing impact oscillations and contributes to a more stable system response under substantial impact loads, thereby improving the stability of the dynamic capture process.

It is worth noting that the nonlinearity of the stiffness and damping can be designed by altering spring stiffness k_s and orifice radius r_0, as shown in Figs. 4 and 5. Optimal stiffness and damping profiles (i.e., optimized structural parameters) for a specific dynamic target can be obtained by defining an appropriate objective function, for example, maximum energy dissipation. Considering the actual components used for the fabrication of the P-VSDR, the main parameters listed in Table III were selected in the simulation and experiment.

To understand the effectiveness of the P-VSDR in impact buffering and energy dissipation, a comparative analysis of the impact contact for two regulators was carried on: (1) The passive constant stiffness-damping regulator (P-CSDR) in which the tendon is directly attached to the linear spring-damper unit. (2) The P-VSDR in which the tendon is attached to the linear spring-damper unit through a nonlinear transmission unit.

For the P-CSDR, the impact force with respect to the slider displacement $\boldsymbol{X}_t$ is shown in Fig. 6(a). The output effective stiffness of 100 N/m (equal to the stiffness of the linear spring) and damping of 0.98 Ns/m on the slider do not change with the slider displacement $\boldsymbol{X}_t$. It can be seen that the maximum impact force is 8.2 N. In the P-VSDR, the output effective stiffness and damping on the slider change in real-time with the slider displacement $\boldsymbol{X}_t$ under the same simulation parameters (see Table III). In this case, the output effective stiffness and damping on the slider gradually approach the P-CSDR stiffness-damping value 100 N/m and 0.98 Ns/m as displacement $\boldsymbol{X}_t$ increases, as shown in Fig. 6(b). The maximum

https://doi.org/10.1017/S0263574725102105 Published online by Cambridge University Press

Table III. *List of simulation parameters in collision.*

Symbol	Description	Value
m_s	Mass of the spring	2 g
m_p	Mass of the piston rod	5 g
r_o	The orifice radius	1.5 mm
R_p	The piston radius	10 mm
r_p	The piston rod radius	2 mm
C_d	The flow coefficient of the hydraulic oil	0.66
ρ	The density of the hydraulic oil	850 kg/m^3
r_{ro}	The radius of the pulley	4 mm
h_{ro}	The distance from the center of the pulley to the centerline of the guide rod	9 mm
$\theta_{b,0}$	The initial angle between the tendon and the guide rod	85 degrees
m_{ta}	Mass of the dynamic target	150 g
$v_{ta,0}$	Initial velocity of the dynamic target	5 m/s

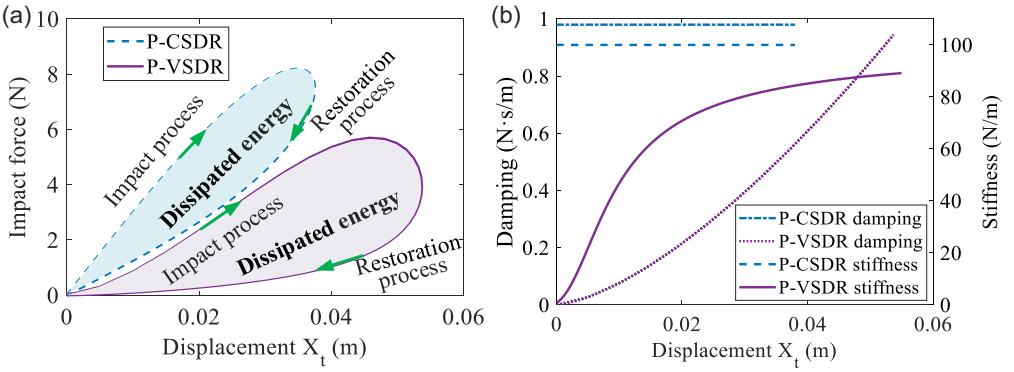


Figure 6. *Simulated comparison of the P-CSDR and P-VSDR. (a) Impact force and dissipated energy. (b) Variation of stiffness and damping in the P-CSDR and P-VSDR, respectively.*

impact force on the slider is reduced to 5.7 N. The area enveloped by the impact and restoration curves indicates the dissipated energy. It is 1.56 J in the P-VSDR while 0.84 J in the P-CSDR, as shown in Fig. 6(a). According to Eq. (6), the energy dissipation efficiency of 83.2% in the P-VSDR is greater than that of 44.8% in the P-CSDR.

By comparing the simulation results in an impact process, it is found that the slider displacement and time in the P-VSDR are greater than that in the P-CSDR, while the impact force and energy dissipation are noticeably better than the results of the P-CSDR.

3.3. Design of the robotic gripper

The robotic gripper developed in this section consists of a tentacle cluster capture mechanism, a deployable mechanism driven by a linear motor that opens and closes the gripper, and the passive nonlinear stiffness and damping regulators, which are shown in Fig. 7(a). Each tentacle is composed of an elastic layer on its ventral side and discrete limiting blocks on its dorsal side, as shown in Fig. 7(b). In comparison to other capture mechanisms (e.g., net, fingered gripper), the use of a tentacle cluster can achieve an omni-directional envelope to the dynamic target [26] and therefore improve the fault tolerance in the capture process.

https://doi.org/10.1017/S0263574725102105 Published online by Cambridge University Press

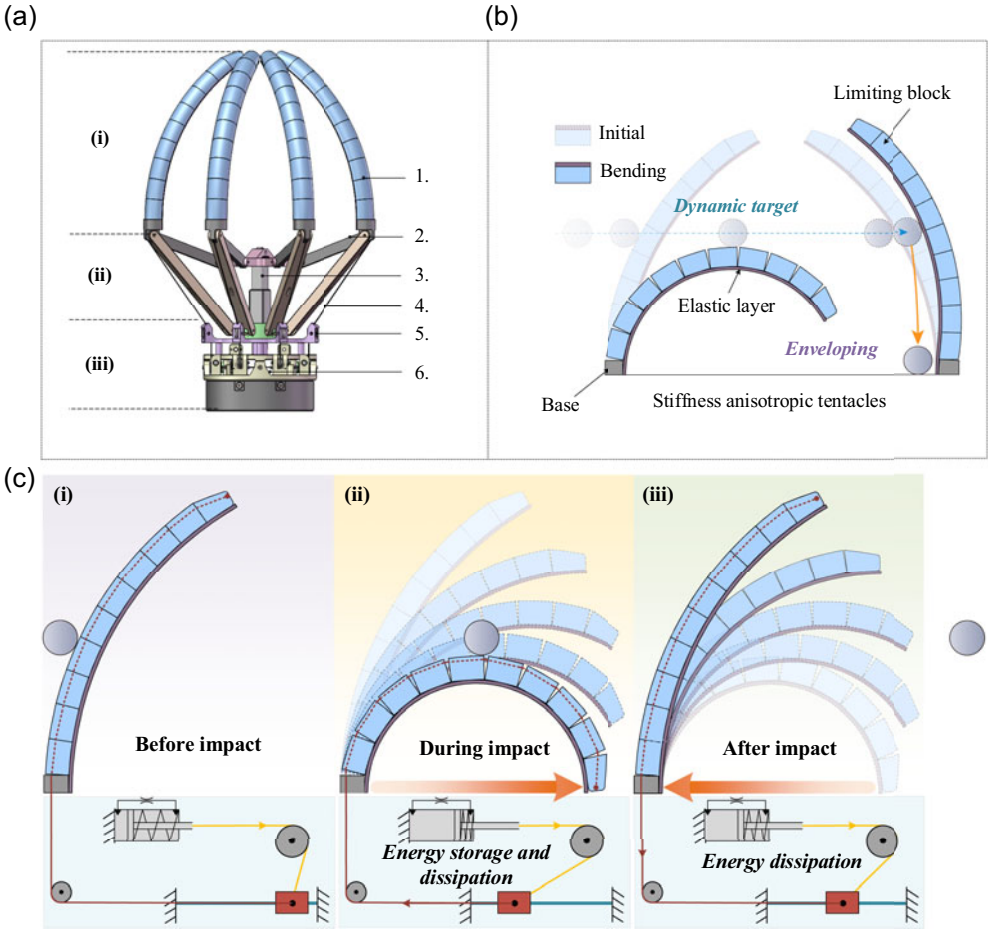


Figure 7. *Prototype of the robotic gripper. (a) The robotic gripper is mainly composed of (i) a cluster capture mechanism, (ii) a deployable mechanism, and (iii) the passive variable stiffness and damping regulators. 1. The tentacles 2. Links base. 3. Linear motor 4. Tendon 5. Guide pulley 6. P-VSDR. (b) Concept of the tentacle cluster with stiffness anisotropy and its strategy for capturing dynamic targets. (c) Three stages of the robotic gripper are (i) before the impact, (ii) during the impact, and (iii) after the impact and impact energy buffering and energy dissipation principles.*

In this section, we integrate the proposed P-VSDR into the tentacle by connecting the tendon of the tentacle to the slider of the P-VSDR, as shown in Fig. 7(c). There are three states of the P-VSDR following the deformation of the tentacle:

1. Before the impact on the tentacle, the P-VSDR and the tentacles maintain the initial state, and stiffness and damping of the P-VSDR do not change, as shown in Fig. 7(c-i).
2. During the impact, the tentacles start bending, and the tension on the tendon increases. The impact force is transmitted through the tendon to the P-VSDR, which buffers the impact force to reduce the speed of the dynamic target, as shown in Fig. 7(c-ii). A part of the kinetic energy of the dynamic target is stored in the compressed spring within the hydraulic cylinder and the elastic deformation of the tentacle. The rest kinetic energy is dissipated through the damping orifice.

https://doi.org/10.1017/S0263574725102105 Published online by Cambridge University Press

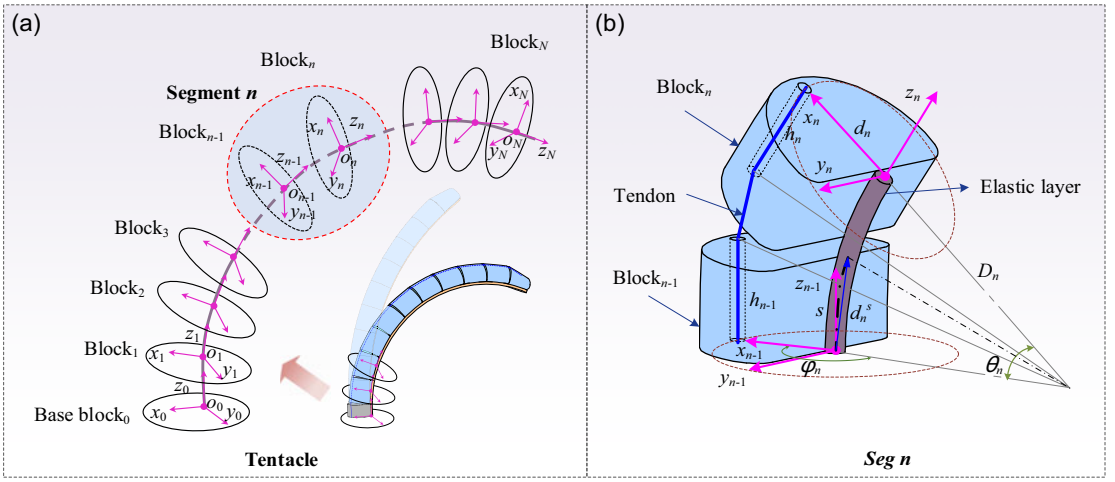


Figure 8. *Kinematic model of the tentacle. (a) Frames of blocks and elastic layer. (b) Relationship between driving cables and routing holes.*

3. After the impact, the tentacle goes back to its initial position, and the tension on the tendon decreases. The energy stored in the spring and tentacle is released, leading to the reverse movement of the slider, and eventually dissipated by the orifice, as shown in Fig. 7(c-iii).

This regulator can passively vary the stiffness and damping level to accommodate the impact forces, eliminating the need for complex active sensing and feedback control. When contact just occurs, characterized by low impact, the tentacle operates in a low stiffness and damping configuration. This ensures safe engagement with the target while minimizing rebound. Then, both stiffness and damping gradually increase to prolong the interaction time. This effectively reduces peak impact forces and enhances energy dissipation.

4. Modeling of the robotic gripper equipped with P-VSDR

In this section, a dynamic model of the robotic gripper equipped with P-VSDR is established to analyze the impact buffering and energy dissipation behaviors.

4.1. Kinematic model of the tentacle

The limiting block n ($n = 1, 2, 3, \ldots,$ n) on a tentacle is denoted as block$_n$, where block$_0$ denotes the base. As shown in Fig. 8(a), block$_{n-1}$, block$_n$, and the elastic layer constitute a microelement segment n, referred to as Seg_n. The spatial frame o_0-$x_0y_0z_0$ is fixed at the center of the base. A series of local frames o_n-$x_ny_nz_n$ and o_{n-1}-$x_{n-1}y_{n-1}z_{n-1}$ are established at the location of the fixed point where each limiting block is connected to the elastic layer [26], as shown in Fig. 8(b). In each local frame, the x direction points to the position of the tendon hole, the y direction is parallel to the direction of the elastic layer, and the z direction is tangent to the equivalent spatial curve of the elastic layer.

Screw theory is utilized to provide an intuitive and concise description of the motion of the tentacle [44–47]. The analytic model of the proposed tentacle is deduced in Appendix A, where the theoretical explanation of the abovementioned kinematics is presented.

The transformation matrix of exponentials (POE) formula from the base to the impact Seg_n of the tentacle is expressed as

$$e^{\theta_n \cdot \hat{\xi}_n} = \begin{bmatrix} r_n & p_n \\ \mathbf{0} & 1 \end{bmatrix} \in SE(3) \tag{14}$$

https://doi.org/10.1017/S0263574725102105 Published online by Cambridge University Press

The POE transformation matrix of the impact Seg_n relative to the spatial frame can be computed as follows:

$$T_{n,k}(q) = \left(\prod_{m=1}^{n-1} e^{\theta_m \cdot \hat{\xi}_m}\right) \cdot e^{\theta_n \cdot \hat{\xi}_n} T_n(0) = \begin{bmatrix} R_{n,k} & P_{n,k} \\ \mathbf{0} & 1 \end{bmatrix}, k \in [0, L], n = 1, 2 \cdots N_{Seg} \tag{15}$$

where $e^{\theta_n \cdot \hat{\xi}_n} \in SE(3)$ is the screw motion of the Seg_n, $\hat{\boldsymbol{\xi}}_n$ is the twist of the Seg_n with respect to the $Seg_{n\text{-}1}$, $\boldsymbol{\xi}_n$ is the twist frame of the motion of the Seg_n., and $\boldsymbol{T}$ (0) is the initial position and orientation of the tentacle at time 0.

When a dynamic target impacts the Seg_n of the tentacle, the Seg_n is deformed to form a constant-curvature mini-arc. The radius of this mini-arc is

$$D_n = \frac{l_{Seg}}{\theta_n} \tag{16}$$

Based on the deformed parameters of the elastic layer, the value of the change in the length of the tendon on Seg_n can be obtained as follows:

$$te_n = \left[2 \sin\left(\frac{\theta_n}{2} - \arctan\frac{L_{te} + d_n\theta_{te,0}}{2N(d_n + D_n)}\right)\sqrt{\left(\frac{L_{te} + d_n\theta_{te,0}}{2N}\right)^2 + (d_n + D_n)^2}\right]\cos(\varphi_n)^{-1} \tag{17}$$

where d_n is the distance from the tendon hole to the position of the frame center axis and $\theta_{te,0}$ is the initial deformation angle of the elastic layer.

The value of the total length change of the tendon is a function of the parameters $\boldsymbol{\theta} = [\theta_1\ \theta_2 \cdots \theta_n \cdots \theta_N]^T$ and $\boldsymbol{\varphi} = [\varphi_1\ \varphi_2 \cdots \varphi_n \cdots \varphi_N]^T$ with respect to the spatial configuration of the tentacle as follows:

$$X_t(\boldsymbol{\theta}, \boldsymbol{\varphi}) = \sum_{n=1}^{N} te_n \tag{18}$$

4.2. Dynamic model of the tentacle

Assuming all tentacles have the same structure, in the model, we take a single tentacle as an example to analyze the contact dynamics. The tentacle will bend inward after being impacted by the dynamic target. Therefore, it is necessary to develop a dynamic model for the tentacle to judge whether the target can pass through the tentacles and be captured. Meanwhile, the established dynamic model can also be used to analyze the impact buffering and energy dissipation capabilities during the collision. In this section, an effective dynamic model based on the principle of virtual power is established [48, 49], which can achieve the calculation and simulation of impact force buffering and energy dissipation.

In this section, a contact dynamic model of the tentacle is established based on the principle of virtual power, which is presented in Appendix B. According to the forces of the tentacle that may be suffered, the virtual power equation of the system can be written as

$$\delta P_b^I + \delta P_e^I + \delta P_e + \delta P_{te} = \delta P_{g,b} + \delta P_{g,e} + \delta P_{imp} \tag{19}$$

Equation (19) can be rewritten as

$$\delta\dot{q}^{\mathrm{T}}\left((M_b + M_e)\ddot{q} + F_e + F_{te} - Q_{g,b} - Q_{g,e} - Q_{imp}\right) = 0 \tag{20}$$

$$M = M_b + M_e \tag{21}$$

where $\boldsymbol{M}$ represents the generalized mass matrix.

https://doi.org/10.1017/S0263574725102105 Published online by Cambridge University Press

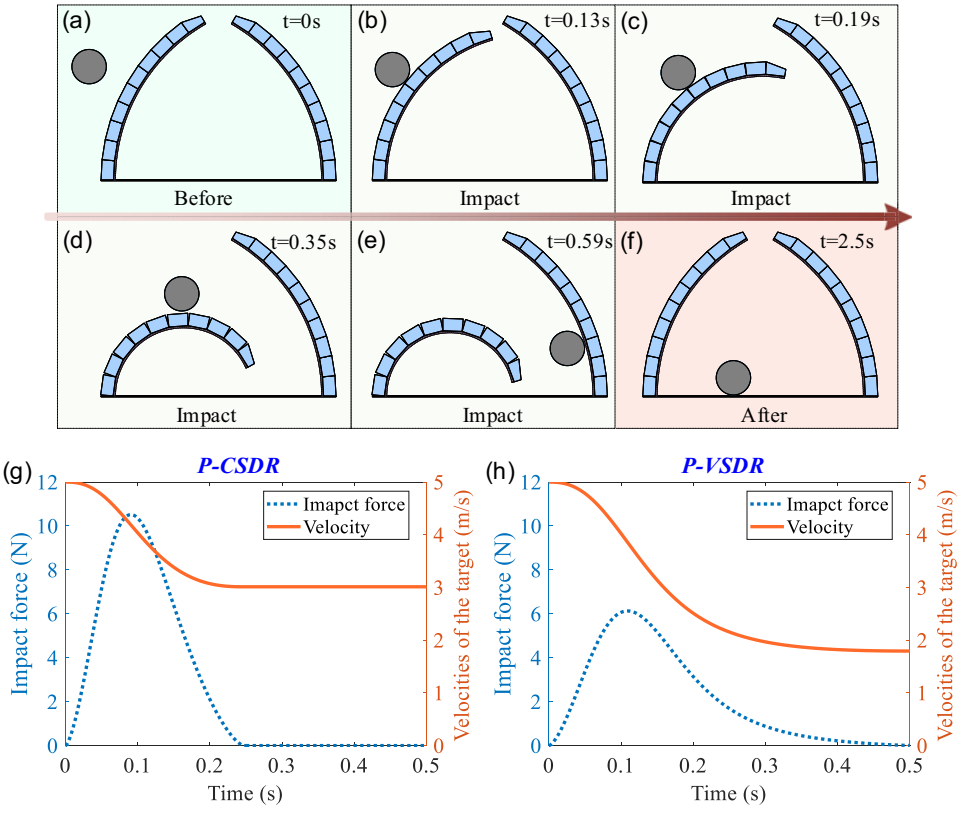


Figure 9. *Simulation of the capture process. (a) Before the impact. (b)–(e) During the impact. (f) After the impact. (g) Impact force and target velocity when using the tentacle equipped with P-CSDR. (h) Impact force and target velocity when using the tentacle equipped with P-VSDR.*

The contact dynamics of the whole system when a dynamic target with mass m impacts a tentacle is calculated as

$$\begin{cases} m\ddot{P}_{n,k} + F_{imp} = 0 \\ M\ddot{q} + F_e + F_{te} - Q_{g,b} - Q_{g,e} - Q_{imp} = 0 \\ P_{n,k}(0) = 0, \dot{P}_{n,k}(0) = v_{ta,0} \\ q(0) = 0, \dot{q}(0) = 0 \end{cases} \tag{22}$$

4.3. Simulation validation of the robotic gripper

In this section, the impact between the gripper and dynamic target in a plane is illustrated by simulation. Figure 9(a)–(f) depicts the dynamic target capture process involving a pair of tentacles equipped with P-VSDR:

(a) Before contact, the dynamic target is approaching the tentacle, which is in its initial state.

(b) Initial contact occurs when the dynamic target hits the dorsal side of one tentacle.

(c) The tentacle starts bending, and the impact force is relatively low; thus, the P-VSDR system responds with low stiffness and damping to gently absorb the initial impact.

(d) As the deformation of the tentacle and the impact force increases, the P-VSDR generates high stiffness and damping configuration to manage the growing impact forces.

https://doi.org/10.1017/S0263574725102105 Published online by Cambridge University Press

(e) After the dynamic target has decelerated, it is intercepted by the ventral side of the other tentacle and falls into the gripper.

(f) The capture is completed, and the tentacles return to their initial state.

This sequence demonstrates the adaptive nature of the tentacle equipped with a P-VSDR, which can passively modulate its stiffness and damping.

Figure 9(g) and (h) shows the variations of impact force and target velocity by using the tentacle equipped with P-CSDR and P-VSDR, respectively. The dynamic target used for simulation has an initial velocity of 5 m/s, a radius of 15 mm, and a mass of 150 g. The entire process is in video S1 of the supplementary materials. It can be seen in Fig. 9(g) that the maximum impact force was 10.52 n with a target velocity of 3.01 m/s and the interaction time duration is 0.25 s. The energy dissipation efficiency, calculated with Eq. (6), was 63.76%. In contrast, Fig. 9(h) presents the results for a tentacle equipped with a P-VSDR, which results in a reduced maximum impact force of 6.13 n with a target velocity of 1.79 m/s, and the interaction lasts 0.5 s. The P-VSDR achieved a significantly higher energy dissipation efficiency of 87.18%. This comparative analysis of the simulation results shows the impact mitigation and energy dissipation capabilities of the P-VSDR-equipped tentacle, which are critical for the capture of dynamic targets.

5. Experimental validations

In this section, a series of experiments were carried out to evaluate the impact buffering and energy dissipation performance of tentacles equipped with P-VSDR.

Figure 10(a) shows a robotic gripper with tentacles uniformly arranged in a circular pattern, designed to form a "trap" for dynamic targets approaching from any direction. Eight P-VSDRs are mounted on the bottom of the tentacles accordingly. To provide a comparative analysis, the P-VSDR can be replaced by the P-CSDR as shown in Fig. 10(b).

Figure 10(c) provides a schematic of the experimental setup, including the tentacle and a target launcher. The movement of the marker ball was recorded by a dynamic capture system (Mars1.3HW, NOKOV Science & Technology Co., Ltd.). The frame rate was set to 100 fps, and the resolution was 1280 × 1024 PPI.

5.1. Impact contact of the tentacle

Figure 11 illustrates a series of demonstrations involving a marker ball with a diameter of 20 mm and a mass of 115 g. The ball is propelled toward the tentacle with impact velocities of 1 m/s, 1.5 m/s, and 2 m/s. The term "impact time" refers to the moment when the marker ball makes contact with the tentacle for the first time, while "separation time" means the instant when the ball ceases contact and detaches from the tentacle. The time interval between them is defined as the "duration of contact."

In Fig. 11(a), the initial high stiffness and damping of the P-CSDR result in quick contact and separation, causing the marker ball to rebound after impact. This behavior indicates a shorter interaction time and a higher peak force. In Fig. 11(b), the variable stiffness and damping of the P-VSDR extend the duration of contact, reducing the peak impact force and enabling smooth energy dissipation. It can be seen that the rebound of the marker ball is reduced as well.

Figure 11(c) provides the velocity profiles of the marker ball with impact velocities of 1 m/s, 1.5 m/s, and 2 m/s. It can be seen that the marker ball experiences a rapid velocity reduction at impact time in the case of P-CSDR. In contrast, if the P-VSDR is utilized, the marker ball exhibits velocity oscillations when contact occurs due to the low damping of the tentacle. These oscillations will be suppressed as the damping value increases. Furthermore, the variable stiffness prolongs the duration of contact between the marker ball and the tentacle. Video S2 in the supplementary materials shows the experiment process.

Figure 11(d) presents the duration of contact for the tentacle equipped with P-CSDR and P-VSDR, respectively, at impact velocities of 1 m/s, 1.5 m/s, and 2 m/s. The duration of contact for the tentacle equipped with P-CSDR is 350 ms, 270 ms, and 220 ms, whereas 640 ms, 590 ms, and

https://doi.org/10.1017/S0263574725102105 Published online by Cambridge University Press

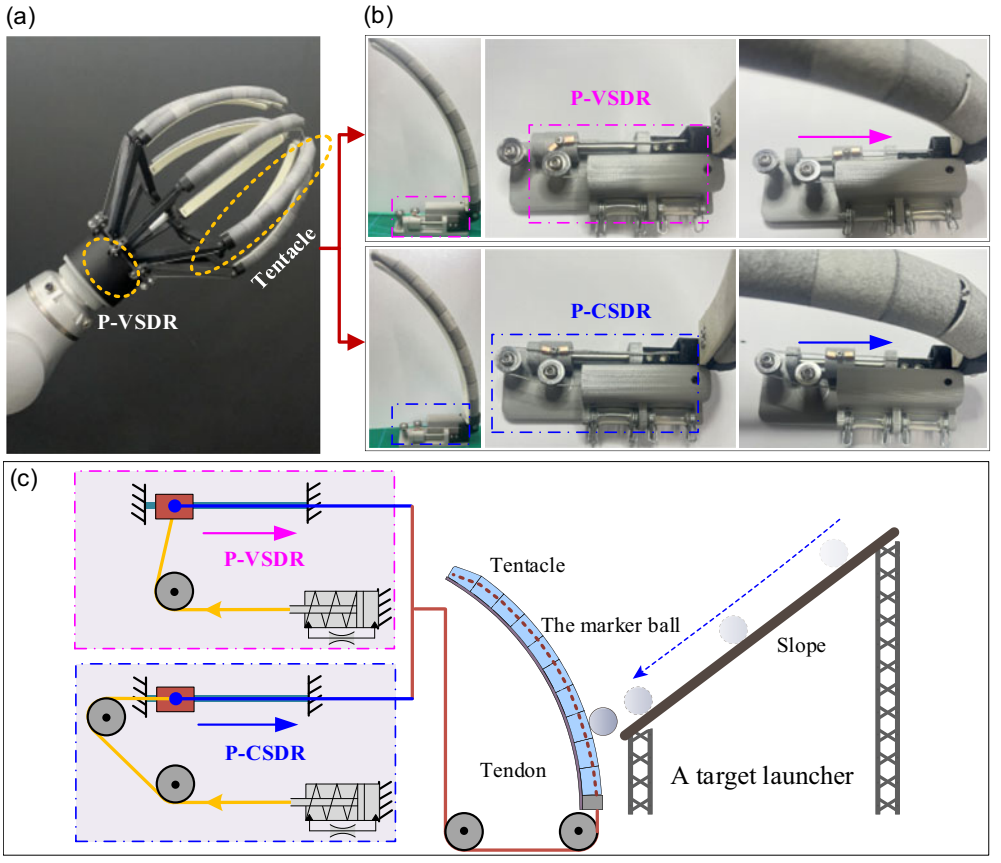


Figure 10. *Experimental platform for evaluating contact dynamics between a dynamic target and tentacles equipped with P-VSDR and P-CSDR. (a) The robotic gripper composed of tentacles with modular design. (b) Tentacles of the same structure are connected to P-VSDR and P-CSDR, respectively. (c) The experimental setup.*

480 ms for the tentacle equipped with P-VSDR. These results show the capability of the P-VSDR to mitigate peak impact forces by prolonging the duration of contact. The extended duration of contact also provides the gripper more time to capture dynamic targets, thereby improving the success rate of the capture.

Figure 11(e) presents the energy dissipation efficiency of the tentacle integrated with P-CSDR and P-VSDR at impact velocities of 1 m/s, 1.5 m/s, and 2 m/s. According to Eq. (6), the P-CSDR achieves energy dissipation efficiencies of 60.31%, 59.04%, and 60.93%, respectively, with an average efficiency of 60%. In contrast, the P-VSDR achieves efficiencies of 68.64%, 83.46%, and 86.68%, with an average of 80%. These experimental results are consistent with the simulated results obtained from the dynamics model presented in Section 4.3. Notably, the P-VSDR enables a more efficient energy dissipation process, particularly for the target with high initial velocity.

5.2. Potential applications

In this section, the gripper was mounted on a continuum robot, as shown in Fig. 12(a), to demonstrate its dynamic capture capability.

Figure 12(b) presents a demonstration of capturing a polyhedral target with a diameter of 82 mm and a mass of 116 g. The target was launched at initial velocities of 3 m/s, 4 m/s, and 5 m/s, with 20

https://doi.org/10.1017/S0263574725102105 Published online by Cambridge University Press

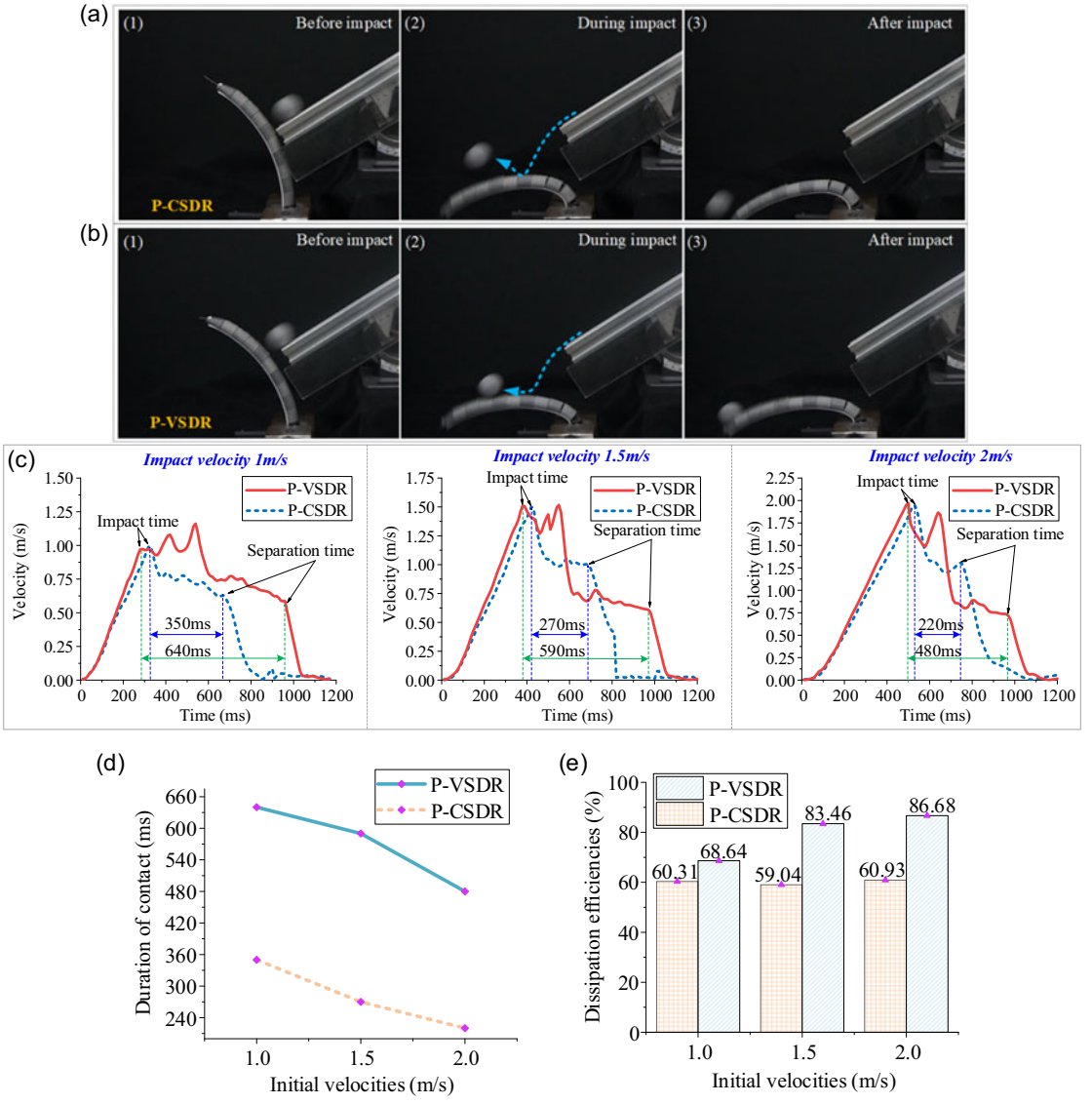


Figure 11. *A marker ball hit the tentacle equipped with P-CSDR and P-VSDR at impact velocities of 1 m/s, 1.5 m/s, and 2 m/s. (a) The contact process by using the P-CSDR with constant stiffness and damping. (b) The contact process by using the P-VSDR with variable stiffness and damping. (c) The velocity profiles of the marker ball. (d) The duration of contact. (e) The energy dissipation efficiency.*

capture attempts made at each velocity, achieving success rates of 90%, 95%, and 95%, respectively. Supplementary Video S3 illustrates that the gripper does not require precise trajectory measurement of the target; it only needs to intercept the dynamic target by putting the gripper approximately on the path of the target [26].

Another demonstration is to capture a drone. As shown in Fig. 12(c) and Supplementary Video S4, the drone, flying at velocities of 3 m/s, 6 m/s, and 9 m/s, was successfully captured. Twenty attempts were made at each speed, resulting in success rates of 60%, 75%, and 90%. This positive correlation between dynamic target velocity and success rate may be attributed to the enhanced kinetic energy at higher speeds, which helps the drone effectively travel through the tentacles of the

https://doi.org/10.1017/S0263574725102105 Published online by Cambridge University Press

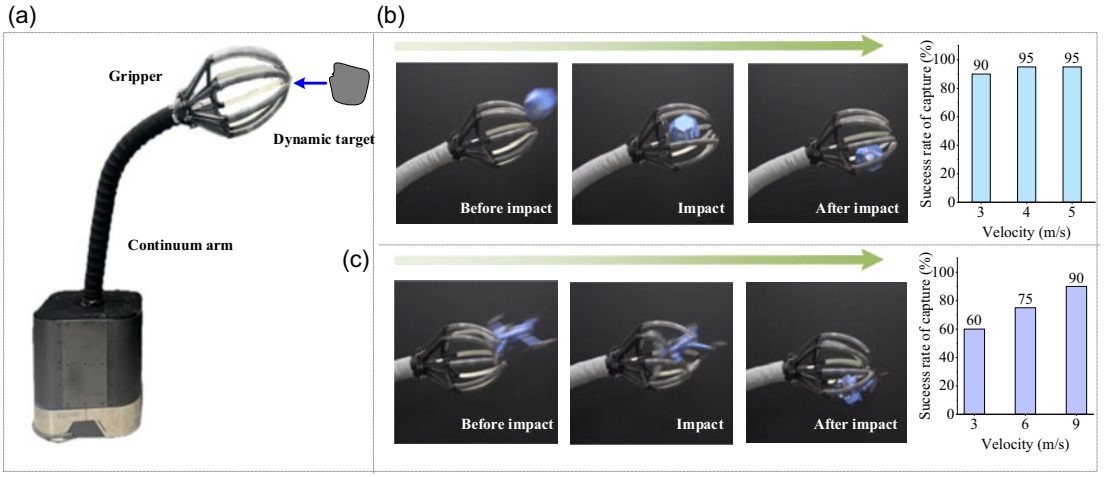


Figure 12. *The robotic gripper captures demonstrations. (a) Gripper mounted on a continuum arm. (b) Capturing a polyhedron. (c) Capturing a drone.*

gripper. This demonstration confirms the feasibility of utilizing the gripper for capturing dynamic targets.

6. Conclusion and discussion

This study addressed the challenges of dynamic capture by introducing a novel robotic gripper equipped with a P-VSDR. Unlike conventional rigid grippers that risk impact damage or rely on complex sensing and control systems and traditional soft grippers lacking of stiffness and damping for impact buffering, the proposed gripper offers a tailored approach to adjust the stiffness and damping during the contact.

By analyzing the Kelvin–Voigt and Hunt–Crossley models, it was found that reducing stiffness and damping at the initial stage of contact can minimize impact force, preventing the target from rebound. Then, increasing stiffness and damping at the later stage of contact will guarantee sufficient strength for capturing the target and dissipating kinetic energy.

The P-VSDR encapsulates this strategy by adopting a nonlinear tendon-driven transmission unit. Through simulations and experiments, it was validated that the P-VSDR effectively prolongs the duration of contact and reduces the peak impact force. As a result, the energy dissipation efficiency reaches 86.68%, which has a significant improvement in comparison to the one using constant stiffness and damping.

The passive mechanism used in this paper is suitable for tasks where rapid response and system reliability are priority, for example, capturing a dynamic target. Our future work will investigate active control based on the electric controller and sensors, enhancing system adaptability to deal with various scenarios and conditions.

Supplementary material. The supplementary material for this article can be found at https://doi.org/10.1017/S0263574725102105.

Author contribution. Conceptualization: S.Y., R.K.; methodology: S.Y., R.K.; validation: S.K., Z.S., R.K.; formal analysis: S.K.; investigation: S.K.; resources: R.K.; data curation: S.Y.; writing and review: S.K., Z.S., D.B., T.S., J.S., R.K.; supervision: R.K.; project administration: T.S., R.K.; and funding acquisition: J.D., R.K.

Financial support. This work was supported by the National Natural Science Foundation of China, Project No. 52375023.

Conflicts of interest. The authors declare none.

https://doi.org/10.1017/S0263574725102105 Published online by Cambridge University Press

References

[1] C. Yang, I. D. Walker, D. T. Branson, J. S. Dai, T. Sun and R. Kang, "A multi-tentacle gripper for dynamic capture," *IEEE Trans. Robot.* **40**, 4284–4300 (2024).

[2] C. Laschi, B. Mazzolai and M. Cianchetti, "Soft robotics: Technologies and systems pushing the boundaries of robot abilities," *Sci. Robot.* **1**(1), eaah3690 (2016).

[3] Y. Zhang, W. Zhang, P. Gao, X. Zhong and W. Pu, "Finger-palm synergistic soft gripper for dynamic capture via energy harvesting and dissipation," *Nat. Commun.* **13**(1), 7700 (2022).

[4] Z. Xie, F. Yuan, J. Liu, L. Tian, B. Chen, Z. Fu, S. Mao, T. Jin, Y. Wang, X. He, G. Wang, Y. Mo, X. Ding, Y. Zhang, C. Laschi and L. Wen, "Octopus-inspired sensorized soft arm for environmental interaction," *Sci. Robot.* **8**(84), eadh7852 (2023).

[5] P. H. Kuo and A. D. Deshpande, "Muscle-tendon units provide limited contributions to the passive stiffness of the index finger metacarpophalangeal joint," *J. Biomech.* **45**(15), 2531–2538 (2012).

[6] Z. Song, S. Lan and J. S. Dai, "A new mechanical design method of compliant actuators with non-linear stiffness with predefined deflection-torque profiles," *Mech. Mach. Theory* **133**, 164–178 (2019).

[7] X. Hu, Z. Song and T. Ma, "Novel design method for nonlinear stiffness actuator with user-defined deflection-torque profiles," *Mech. Mach. Theory* **146**, 103712 (2020).

[8] F. Liu, F. Sun, B. Fang, X. Li, S. Sun and H. Liu, "Hybrid robotic grasping with a soft multimodal gripper and a deep multistage learning scheme," *IEEE Trans. Robot.* **39**(3), 2379–2399 (2023).

[9] Y. B. Jia, M. Gardner and X. Mu, "Batting an in-flight object to the target," *Int. J. Robot. Res.* **38**(4), 451–485 (2019).

[10] N. Marturi, M. Kopicki, A. Rastegarpanah, V. Rajasekaran, M. Adjigble, R. Stolkin and Y. Bekiroglu, "Dynamic grasp and trajectory planning for moving objects," *Auton. Robot.* **43**, 1241–1256 (2019).

[11] S. Kim, A. Shukla and A. Billard, "Catching objects in flight," *IEEE Trans. Robot.* **30**(5), 1049–1065 (2014).

[12] B. V. Vidyadhara, L. A. Tony, M. S. Gadde, S. Jana, V. P. Varun, A. A. Bhise, S. Sundaram and D. Ghose, "Design and integration of a drone based passive manipulator for capturing flying targets," *Robotica* **40**(7), 2349–2364 (2022).

[13] P. Huang, D. Wang, Z. Meng and Z. Liu, "Post-capture attitude control for a tethered space robot–target combination system," *Robotica* **33**(4), 898–919 (2015).

[14] F. Stroppa, F. J. Majeed, J. Batiya, E. Baran and M. Sarac, "Optimizing soft robot design and tracking with and without evolutionary computation: An intensive survey," *Robotica* **42**(8), 2848–2884 (2024).

[15] D. Rus and M. T. Tolley, "Design, fabrication and control of soft robots," *Nature* **521**(7553), 467–475 (2015).

[16] T. T. Michael, F. S. Robert, C. G. Kevin, J. W. Robert and M. W. George, "A resilient, untethered soft robot," *Soft Robot.* **1**(3), 213–223 (2014).

[17] Y. Lee, W. J. Song and J. Y. Sun, "Hydrogel soft robotics," *Mater. Today Phys.* **15**, 100258 (2020).

[18] T. J. Wallin, J. Pikul and R. F. Shepherd, "3D printing of soft robotic systems," *Nat. Rev. Mater.* **3**(6), 84–100 (2018).

[19] B. Chen, Z. Chen, X. Chen, S. Mao, F. Pan, L. Li, W. Liu, H. Min, X. Ding, F. Sun and L. Wen, "Teleoperation of an anthropomorphic robot hand with a metamorphic palm and tunable-stiffness soft fingers," *Soft Robot.* **11**(3), 508–518 (2024).

[20] G. Li, T. W. Wong, B. Shih, C. Guo, L. Wang, J. Liu, T. Wang, X. Liu, J. Yan, B. Wu, F. Yu, Y. Chen, Y. Liang, Y. Xue, C. Wang, S. He, L. Wen, M. T. Tolley, A. M. Zhang, C. Laschi and T. Li, "Bioinspired soft robots for deep-sea exploration," *Nat. Commun.* **14**(1), 7097 (2023).

[21] R. Chen, Z. Yuan, J. Guo, L. Bai, X. Zhu, F. Liu, H. Pu, L. Xin, Y. Peng, J. Luo, L. Wen and Y. Sun, "Legless soft robots capable of rapid, continuous, and steered jumping," *Nat. Commun.* **12**(1), 7028 (2021).

[22] D. Trivedi, C. D. Rahn, W. M. Kier and I. D. Walker, "Soft robotics: Biological inspiration, state of the art, and future research," *Appl. Bionics Biomech.* **5**(3), 99–117 (2008).

[23] N. R. Sinatra, C. B. Teeple, D. M. Vogt, K. K. Parker, D. F. Gruber and R. J. Wood, "Ultragentle manipulation of delicate structures using a soft robotic gripper," *Sci. Robot.* **4**(33), eaax5425 (2019).

[24] Y. Lin, C. Zhang, W. Tang, Z. Jiao, J. Wang, W. Wang, Y. Zhong, P. Zhu, Y. Hu, H. Yang and J. Zou, "A bioinspired stress-response strategy for high-speed soft grippers," *Adv. Sci.* **8**(21), 2102539 (2021).

[25] J. Yang, C. Ren, C. Yang, Y. Wang, S. Wan and R. Kang, "Design of a flexible capture mechanism inspired by sea anemone for non-cooperative targets," *Chin. J. Mech. Eng.* **34**(1), 77 (2021).

[26] S. Yang, Y. Zhou, I. D. Walker, C. Yang, D. T. Branson, Z. Song, J. Dai and R. Kang, "Dynamic capture using a traplike soft gripper with stiffness anisotropy," *IEEE-ASME Trans. Mechatron.* **28**(3), 1337–1346 (2022).

[27] J. Shintake, V. Cacucciolo, D. Floreano and H. Shea, "Soft robotic grippers," *Adv. Mater.* **30**(29), 1707035 (2018).

[28] Y. Haibin, K. Cheng, L. Junfeng and Y. Guilin, "Modeling of grasping force for a soft robotic gripper with variable stiffness," *Mech. Mach. Theory* **128**, 254–274 (2018).

[29] Y. Yang, Y. Chen, Y. Li, M. Z. Chen and Y. Wei, "Bioinspired robotic fingers based on pneumatic actuator and 3D printing of smart material," *Soft Robot.* **4**(2), 147–162 (2017).

[30] Y. Liu, X. Liu, Z. Yuan and J. Liu, "Design and analysis of spring parallel variable stiffness actuator based on antagonistic principle," *Mech. Mach. Theory* **140**, 44–58 (2019).

[31] C. Yang, S. Geng, I. D. Walker, D. T. Branson, J. Liu, J. S. Dai and R. Kang, "Geometric constraint-based modeling and analysis of a novel continuum robot with shape memory alloy initiated variable stiffness," *Int. J. Robot. Res.* **39**(14), 1620–1634 (2020).

[32] S. Yang, P. Chen, D. Wang, Y. Yu and Y. Liu, "Design and analysis of a 2-DOF actuator with variable stiffness based on leaf springs," *J. Bionic Eng.* **19**(5), 1392–1404 (2022).

https://doi.org/10.1017/S0263574725102105 Published online by Cambridge University Press

[33] I. Hussain, A. Albalasie, M. I. Awad, K. Tamizi, Z. Niu, L. Seneviratne and D. Gan, "Design and control of a discrete variable stiffness actuator with instant stiffness switch for safe human-robot interaction," *IEEE Access* **9**, 118215–118231 (2021).
[34] J. Fu, Z. Yu, H. Lin, L. Zheng and D. Gan, "A novel variable stiffness compliant robotic link based on discrete variable stiffness units for safe human–robot interaction," *J. Mech. Robot.* **16**(1), 014501 (2024).
[35] S. Kim and A. Billard, "Estimating the non-linear dynamics of free-flying objects," *Robot. Auton. Syst.* **60**(9), 1108–1122 (2012).
[36] W. Wang, J. Wang, Y. Luo, X. Wang and H. Song, "A survey on force sensing techniques in robot-assisted minimally invasive surgery," *IEEE Trans. Haptics* **16**(4), 702–718 (2023).
[37] Y. Liu, K. Luo, S. Wang, X. Song, Z. Zhang, Q. Tian and H. Hu, "A soft and bistable gripper with adjustable energy barrier for fast capture in space," *Soft Robot.* **10**(1), 77–87 (2023).
[38] Y. B. Jia, "Three-dimensional impact: Energy-based modeling of tangential compliance," *Int. J. Robot. Res.* **32**(1), 56–83 (2013).
[39] P. Zhao, J. Liu, Y. Li and C. Wu, "A spring-damping contact force model considering normal friction for impact analysis," *Nonlinear Dyn.* **105**, 1437–1457 (2021).
[40] M. Machado, P. Moreira, P. Flores and H. M. Lankarani, "Compliant contact force models in multibody dynamics: Evolution of the Hertz contact theory," *Mech. Mach. Theory* **53**, 99–121 (2012).
[41] R. Ramírez, T. Pöschel, N. V. Brilliantov and T. Schwager, "Coefficient of restitution of colliding viscoelastic spheres," *Phys. Rev. E* **60**(4), 4465 (1999).
[42] K. Hunt and F. Crossley, "Coefficient of restitution interpreted as damping in vibroimpact," *J. Appl. Mech.* **42**(2), 440 (1975).
[43] P. Flores, "Contact mechanics for dynamical systems: A comprehensive review," *Multibody Syst. Dyn* **54**, 1–51 (2022).
[44] I. D. Walker, "Continuous backbone "continuum" robot manipulators," *Int Sch Res Notices* **2013**(1), 726506 (2013).
[45] J. S. Dai, "Euler–Rodrigues formula variations, quaternion conjugation and intrinsic connections," *Mech. Mach. Theory* **92**, 144–152 (2015).
[46] C. Yang, R. Kang, D. T. Branson, L. Chen and J. S. Dai, "Kinematics and statics of eccentric soft bending actuators with external payloads," *Mech. Mach. Theory* **139**, 526–541 (2019).
[47] X. Ding, Y. Yang and J. S. Dai, "Topology and kinematic analysis of color-changing ball," *Mech. Mach. Theory* **46**(1), 67–81 (2011).
[48] W. S. Rone and P. Ben-Tzvi, "Continuum robot dynamics utilizing the principle of virtual power," *IEEE Trans. Robot.* **30**(1), 275–287 (2013).
[49] Z. Liu, Z. Cai, H. Peng, X. Zhang and Z. Wu, "Morphology and tension perception of cable-driven continuum robots," *IEEE-ASME Trans. Mechatron.* **28**(1,), 314–325 (2022).

Appendix

A. Kinematic model of the tentacle based on screw theory

Assuming that the microsegments are all equal-curvature microarcs, the shape of Seg_n can be expressed in terms of two sets of configuration parameters θ_n and ϕ_n, which form the spatial configuration vectors $\boldsymbol{q}$ of the tentacles as

$$q = \begin{bmatrix} q_1^T & \cdots & q_n^T & \cdots & q_N^T \end{bmatrix}^T \tag{23}$$

where q_n^T is denoted as

$$q_n^T = \begin{bmatrix} \varphi_n & \theta_n \end{bmatrix}^T \tag{24}$$

The tentacle is equivalent to N equal curvature deformed microsegments tangent and connected the top to base, whose elastic layer can be conceptualized as the central backbone of the continuum robot, as shown in Fig. 8(b). The length of the Seg_n elastic layer can be expressed as

$$l_{Seg} = \frac{L_{te}}{N} \tag{25}$$

where L_{te} is the total length of the elastic layer.

Given the axis of rotation ω and point $\boldsymbol{p}$ on the axis, the twist of the circular motion can be obtained. For the Seg_n of the tentacles, the twist of the geometry is expressed as

$$\boldsymbol{\xi}_n = \begin{bmatrix} -\sin\varphi_n & \cos\varphi_n & 0 & 0 & 0 & \frac{l_{Seg}}{\theta_n} \end{bmatrix}^T \tag{26}$$

https://doi.org/10.1017/S0263574725102105 Published online by Cambridge University Press

If the Seg_n of the tentacle is not deformation, the twist of the Seg_n is

$$\boldsymbol{\xi}_n = \begin{bmatrix} 0 & 0 & 0 & 0 & 0 & 1 \end{bmatrix}^T \tag{27}$$

B. Dynamic model of the tentacle based on the principle of virtual power

According to the structure of the tentacle, it can be divided into the limiting block and the elastic layer. The virtual power of the tentacle can be given as follows:

(1) *Virtual Power of the Inertial Force of the Limiting Block:* The virtual power δP_b^I of the inertial force of the limiting block is defined as

$$\delta P_b^I = \sum_{n=1}^{N} \delta \dot{p}_n^{\mathrm{T}} m_{b,n} \ddot{p}_n + \delta \boldsymbol{\omega}_n{}^{\mathrm{T}} \left(J_n^c \dot{\boldsymbol{\omega}}_n + \boldsymbol{\omega}_n \times \left(J_n^c \boldsymbol{\omega}_n \right) \right) = \delta \dot{q}^{\mathrm{T}} \left(M_b \ddot{q} + Q_b \right) \tag{28}$$

where $m_{b,n}$ and J_n^c are the mass and moment of inertia matrix of the Seg_n limiting block, respectively. $\boldsymbol{M}_b$ and $\boldsymbol{Q}_b$ are the mass matrix and inertia force vector of the limiting block, respectively.

(2) *Virtual Power of the Inertial Force of the Elastic Layer:* The virtual power δP_e^I of the inertial force of the elastic layer is defined as

$$\delta P_e^I = \sum_{n=1}^{N} \int_0^{l_{Seg}} \left(\left(\delta \dot{r}_n^s \right)^{\mathrm{T}} \ddot{r}_n^s + \left(\delta \boldsymbol{\omega}_n^s \right)^{\mathrm{T}} \left(J_n^s \dot{\boldsymbol{\omega}}_n^s + \boldsymbol{\omega}_n^s \times \left(J_n^s \boldsymbol{\omega}_n^s \right) \right) \right) \rho_e \mathrm{d}s = \delta \dot{q}^{\mathrm{T}} \left(M_e \ddot{q} + Q_e \right) \tag{29}$$

where the velocity vector $\dot{r}_n^s$ and angular velocity vector ω_n^s of the cross-section at arc length s on the centroid line of the elastic layer of the Seg_n can be obtained. J_n^s denotes the moment of inertia matrix for the elastic layer of the Seg_n with length d_n^s in the deformed configuration. ρ_e is the mass density of the cross-section of the elastic layer. $\boldsymbol{M}_e$ and $\boldsymbol{Q}_e$ are the mass matrix and inertia force vector of the elastic layer of the Seg_n, respectively.

(3) *Virtual Power of Elastic Forces of the Elastic Layer:* The elastic effect of the elastic layer of a tentacle explains the forces and moments generated by deformation within the elastic layer. Therefore, the virtual power of the deformation stress and torsional stress of the elastic layer within this Seg_n is generated as

$$\delta P_e = \frac{EI_{yy}}{l_{Seg}} \sum_{n=1}^{N} \theta_n \delta \dot{\theta}_n + \frac{GI_{zz}}{l_{Seg}} \sum_{n=1}^{N} \varphi_n \delta \dot{\varphi}_n = \delta \dot{q}^{\mathrm{T}} F_e \tag{30}$$

where I_{yy} represents the moment of inertia of the elastic layer cross-section about the neutral axis y, I_{zz} represents the moment of inertia of the elastic layer cross-section about the neutral axis z, E represents the elastic modulus of the elastic layer, G is the shear modulus of the elastic layer, and $\boldsymbol{F}_e$ represents the internal stress vector of the elastic layer.

(4) *Virtual Power of the P-VSDR:* The virtual power of the tension on the tendon caused by the P-VSDR is

$$\delta P_{te} = F_{te} \delta \dot{X}_t = \delta \dot{q}^{\mathrm{T}} F_{te} \tag{31}$$

where $\boldsymbol{F}_{te}$ represents the horizontal force on the slider.

(5) *Virtual Power of Gravity of the Limiting Block:* The center of mass of the limiting block is located at the fixed point where each limiting block is connected to the elastic layer. The virtual power of the gravity of the limiting block is defined by

$$\delta P_{g,b} = \sum_{n=1}^{N} \delta \dot{p}_n{}^{\mathrm{T}} m_{b,n} g = \delta \dot{q}^{\mathrm{T}} Q_{g,b} \tag{32}$$

where $\boldsymbol{Q}_{g,b}$ is the generalized gravity vector of the limiting block.

https://doi.org/10.1017/S0263574725102105 Published online by Cambridge University Press

(6) *Virtual Power of Gravity of the Elastic Layer:* The virtual power of the gravity of the elastic layer is defined by

$$\delta P_{g,e} = \sum_{n=1}^{N} \int_{0}^{l_{Seg}} \left(\delta \dot{r}_n^s\right)^{\mathrm{T}} \rho_e \mathrm{g} \mathrm{d}s = \delta \dot{q}^{\mathrm{T}} Q_{g,e} \tag{33}$$

where $\boldsymbol{Q}_{g,e}$ is the generalized gravity vector of the elastic layer.

(7) *Virtual Power of External Impact force:* A concentrated impact force $\boldsymbol{F}_{imp}$ acting on the centroid line at arc length k can be transformed into a distributed force $\boldsymbol{F}_{imp,d} = \boldsymbol{F}_{imp}\ \delta_k(s\text{-}L_k)$ by introducing the *Dirac delta* function. Thus, the virtual power of external impact force can be calculated by

$$\delta P_{imp} = \sum_{n=1}^{N} \int_{o}^{l_{Seg}} \left(\delta \dot{r}_n^s\right)^{\mathrm{T}} F_{imp,d} \mathrm{d}s = \delta \dot{q}^{\mathrm{T}} Q_{imp} \tag{34}$$

where $\boldsymbol{Q}_{imp}$ is the generalized external impact force vector.

Cite this article: S. Yang, Z. Song, D. T. Branson, T. Sun, J. S. Dai and R. Kang (2025). "Robotic gripper for dynamic capture using passive variable stiffness and damping regulator (P-VSDR)", Robotica **43**, 3155–3175. https://doi.org/10.1017/S0263574725102105

https://doi.org/10.1017/S0263574725102105 Published online by Cambridge University Press